scientific reports

Check for updates

OPEN

Statistical computation for heat and mass transfers of water-based nanofluids containing Cu, Al$_2$O$_3$, and TiO$_2$ nanoparticles over a curved surface

Showkat Ahmad Lone[1], Zehba Raizah[2], Anwar Saeed[3] & Gabriella Bognár[4]✉

Nanofluid is a specially crafted fluid comprising a pure fluid with dispersed nanometer-sized particles. Incorporation these nanoparticles into pure fluid results in a fluid with improved thermal properties in comparison of pure fluid. The enhanced properties of nanofluids make them highly sought after, in diverse applications, consisting of coolant of devices, heat exchangers, and thermal solar systems. In this study hybrid nanofluid consisting of copper, alumina and titanium nanoparticles on a curved sheet has investigated with impact of chemical reactivity, magnetic field and Joule heating. The leading equations have converted to normal equations by using appropriate set of variables and has then evaluated by homotopy analysis method. The outcomes are shown through Figures and Tables and are discussed physically. It has revealed in this study that Cu-nanofluid flow has augmented velocity, temperature, and volume fraction distributions than those of Al$_2$O$_3$-nanofluid and TiO$_2$-nanofluid. Also, the Cu-nanofluid flow has higher heat and mass transfer rates than those of Al$_2$O$_3$-nanofluid and TiO$_2$-nanofluid.

List of symbols

(R, S)	Curvilinear coordinates (m)
$u_w = aS$	Stretching velocity (m s^{-1})
a	Positive fixed number (–)
T_f	Surface temperature (K)
ρ	Density (kg m^{-3})
σ	Electrical conductivity (S m^{-1})
C_p	Specific heat capacity (J K^{-1} Kg^{-1})
C_w	Surface volumetric fraction distribution (mol m^{-3})
k	Thermal diffusion (W m^{-1} K^{-1})
δ	Curvature factor (–)
M	Magnetic parameter (–)
Ec	Eckert number (–)
Bi	Thermal Biot number (–)
γ	Chemical reactivity factor (–)
N_b, N_t	Brownian and thermophoresis factors (–)
Sc	Schmidt number (–)

[1]Department of Basic Sciences, College of Science and Theoretical Studies, Saudi Electronic University, (Jeddah-M), 11673 Riyadh, Kingdom of Saudi Arabia. [2]Department of Mathematics, College of Science, Abha, King Khalid University, Abha, Kingdom of Saudi Arabia. [3]Department of Mathematics, Abdul Wali Khan University, Mardan 23200, Khyber Pakhtunkhwa, Pakistan. [4]Institute of Machine and Product Design, University of Miskolc, Miskolc-Egyetemváros 3515, Hungary. ✉email: gabriella.v.bognar@uni-miskolc.hu

Nanofluid is a specialized engineered fluid comprising a base fluid with dispersed nanometer-sized particles. Introducing these nanoparticles in pure fluid enhances its thermal properties compared to the original fluid as first introduced by Choi and Eastman[1]. The enhanced properties of nanofluids make them highly sought after, in diverse applications, consisting of devices coolant, and thermal solar systems[2,3]. This dynamic field continues to evolve as scientists work towards optimizing nanofluid formulations for practical implementation in a range of thermal management scenarios. Heat transfer in nanofluid flows is characterized by the remarkable improvement in thermal conductivity conferred by nanometer-sized particles mixed in pure fluid[4]. Arshad et al.[5] used hybrid nanofluid flow through two gyrating surfaces with impacts of chemical reactivity and thermally radiated effects. The presence of these nanoparticles significantly enhances convective heat transfer, making nanofluids attractive for applications demanding efficient thermal management. The nanoparticle size plays a pivotal role, with smaller particles generally contributing to more effective heat transfer[6]. Nanofluids are particularly valuable in cooling systems for electronics, where their superior heat dissipation properties help prevent overheating. The temperature dependency of thermal conductivity, along with the influence on thermal boundary layers near surfaces, is carefully considered for optimizing performance. Despite the promising advantages, challenges such as nanoparticle stability and uniform dispersion remain subjects of ongoing research, reflecting the evolving nature of utilizing nanofluids to enhance heat transfer in various applications[7]. Arshad et al.[8] explored mass and thermal transportations with first order chemically reactive effects on a dual elongating sheet and conducted a comparative analysis for mono-, bi- and tri-nanoparticles dynamics on flow of fluid. Khan et al.[9] studied irreversibility generation and heat transference for gyrating nanofluid flow on a revolving cylinder and have noticed that velocity panels have deteriorated while thermal panels have escalated with upsurge in nanoparticles volume fraction. Acharya et al.[10] inspected variations in hydrothermal nanofluid flow with impacts of diameter of nanoparticles and nano-layer. Arshad et al.[11] studied time-based mass and thermal transportation on an infinite permeable sheet with impacts of chemical reaction and noticed that growth in Prandtl number has augmented Sherwood and Nussel numbers. Hassan et al.[12] studied numerically the nanofluid flow through two permeable rotary surfaces and noticed that thermal panels have amplified with escalation in nanoparticles number. Arshad et al.[13] used magnetic effects in inclined direction on radiative and chemically reactive nanofluid flow on bi-elongating surface. Hussain et al.[14] modeled mixed convective and visco-elastic nanofluid flow on a circular cylinder with implications of thermal radiations. Nimmy et al.[15] used solar radiations on thermal performance on a wetted fin and observed that thermal panels have deteriorated with expansion in conductive and convective factor as well as with improvement in thermally conductive factor. Khan et al.[16] used the concept of Arrhenius activated energy to study unsteady viscous nanomaterial flow with impacts of bio-convection and slip (partial) constraints.

Magnetohydrodynamic (MHD) fluid flow is a field of physics and engineering that investigates the performance of electrically conducting fluids, such as plasmas and liquid metals, in the existence of magnetic field effects[17]. The fundamental principles of electromagnetism and fluid dynamics are combined into a set of equations, known as the magnetohydrodynamic equations, which describe the complex relationship between fluid motion and magnetic forces. In MHD fluid flow, the Lorentz force emerges from the collaboration amid the magnetic field and charged particles in the fluid, influencing flow patterns, turbulence, and instabilities[18]. This field finds applications in diverse areas, including astrophysics, geophysics, and engineering, with relevance to phenomena such as solar winds, magnetic confinement fusion, and the Earth's magnetic field. MHD fluid flow is essential in the study of technological applications like MHD generators, pumps, and magnetic confinement fusion devices, where the manipulation of fluid motion and magnetic fields holds promise for power generation and propulsion[19]. Sing et al.[20] studied the thermal behavior for magnetized nanofluid flow on an asymmetric conduit filed with Darcy-Brinkman permeable medium. Mahabaleshwar et al.[21] discussed the influences of CNTs on MHD fluid flow on a contracting/extending sheet subject to heat sink/source and thermal radiations. MHD effects can enhance heat transfer, depending on factors such as the strength and orientation of the magnetic field, fluid conductivity, and the nature of the heat source[22]. MHD fluid flow has many applications like in plasma physics, astrophysics, and magnetic confinement fusion, where heat transfer plays a critical role in achieving and maintaining controlled conditions for sustained energy production through nuclear fusion reactions[23]. Hussain et al.[24] computed numerically the optimization of entropy for convective Darcy–Forchheimer nanofluid flow on a flat vertical surface with irregular heat sink/source. Many such studies can be seen in Refs.[25–29].

Brownian motion characterizes the unpredictable and erratic movement of particles suspended in a fluid caused by collisions with neighboring molecules. This phenomenon is particularly significant for nanoparticles and colloidal particles. In Brownian motion, particles experience unpredictable shifts in position, a process driven by thermal energy. Thermophoresis, on the other hand, is a phenomenon in fluid dynamics where suspended particles exhibit a directional motion in reaction to a temperature gradient. When a temperature gradient is present, thermophoresis induces particle migration from regions of lower temperature to higher temperature. Both Brownian motion and thermophoresis play critical roles in nanoparticle transport and assembly, impacting various fields, including nanotechnology, colloidal science, and the design of advanced materials with tailored properties[30,31]. Tawade et al.[32] used these effects (Brownian motion and thermophoresis) for fluid flow on a linearly elongating sheet with impacts of thermal radiations and chemical reactivity. Upreti et al.[33] examined Brownian motion and thermophoresis effects on 3D nanoparticles fluid flow on a Riga plate subject to gyrotactic microorganisms. Brownian motion and thermophoresis significantly influence heat transfer processes, particularly at the nanoscale[34]. Brownian motion, driven by thermal fluctuations, induces random movements of nanoparticles or colloids suspended in a fluid. This stochastic motion enhances convective heat transfer by promoting particle dispersion and reducing thermal boundary layer thickness. Simultaneously, thermophoresis, responding to temperature gradients, imparts directed motion to particles, contributing to heat transfer through particle migration in the fluid. Both phenomena play crucial roles in nanoscale heat conduction, influencing the effective thermal conductivity of nanofluids[35]. In applications like heat exchangers and nanofluidic devices,

understanding and harnessing the relationship between Brownian motion and thermophoresis are essential for optimizing heat transfer efficiency and designing advanced materials with tailored thermal properties[36].

Joule heating, also known as ohmic heating, is a process where electrical energy is converted into heat when an electric current passes through a conductor with some resistance[37]. The phenomenon is named after James Prescott Joule, who first described it in the mid-nineteenth century. Joule heating is prevalent in various electrical devices, such as resistive heaters, electric stoves, and incandescent light bulbs, where the electrical energy is intentionally converted into heat for practical applications[38]. In some cases, particularly in electronic devices and integrated circuits, controlling and minimizing Joule heating is crucial to prevent overheating and ensure the efficient operation of the system. The impact of Joule heating on heat transfer is significant, particularly in electronic devices and conductive materials[39]. In electronic components, this phenomenon can influence the overall thermal management of the device. The heat produced due to Joule heating can lead to temperature gradients and thermal stresses, affecting the performance and reliability of the system[40]. Efficient heat dissipation strategies become crucial to prevent overheating and potential damage. Additionally, in applications like microelectronics and integrated circuits, understanding and managing Joule heating is essential for designing effective cooling systems, heat sinks, and thermal interfaces to enhance overall heat transfer and prevent thermal-induced failures in electronic components. Otman et al.[41] discussed mathematically the analysis of mixed convection stagnant point flow on an extending Riga surface using Joule heating impacts. Irfan et al.[42] inspected thermally on the depiction of mixed convective and radiative nanoparticles flow with Joule heating effects and has proved that thermal transportation has amplified with upsurge in Eckert number. Prakash et al.[43] discussed radiative and bio-convective nanoparticles flow of fluid on extending bi-directional sheet with impacts of Joule heating, modified diffusions and MHD effects.

Thermal convective conditions in fluid flow describe the dynamic process of heat transfer through the movement of a fluid, influenced by temperature gradients. Natural convection occurs when temperature differences induce buoyancy forces, causing the fluid to circulate spontaneously. Forced convection involves externally induced fluid motion, often using pumps or fans, to enhance heat transfer. Mixed convection combines aspects of both natural and forced convection, prevalent in scenarios where external forces and buoyancy both contribute to fluid motion[44]. These thermal convective conditions are pivotal in diverse applications, including the design of heat exchangers, cooling systems, and various industrial processes. The optimization of thermal convective systems requires a comprehensive understanding of fluid behavior, geometry, and external influences, achieved through computational modeling, experimentation, and theoretical analyses[45]. Hamza et al.[46] examined MHD time-dependent flow of fluid with convective constraints at the boundary and have noted that the velocity and thermal distributions have augmented with escalation in Biot number. Rashad et al.[47] inspected Williamson MHD nanofluid flow on a penetrable surface with convective constraints at the boundary and have proved that convective constraints at the boundary and upsurge in thermal radiations has escalated the thermal distribution and declined the velocity panels. Baag et al.[48] studied free convective nanofluid flow on a stretching sheet using the impacts of heat source with heating convective constraints at the boundary. The impact of thermal convective conditions on heat transfer in fluid flow is profound, efficient heat exchange and thermal management in various engineering systems, such as heat exchangers or electronic devices; depend on thermal convective conditions[49]. Prasad et al.[50] studied nanofluid couple stress flow with convective constraints at the boundary using temperature-based characteristics and impacts of MHD.

In this study hybrid nanofluid consisting of copper, alumina and titanium nanoparticles on a curved surface has investigated with impact of chemical reactivity, magnetic field and Joule heating. The leading equations have converted to normal equations by using appropriate set of variables. The purpose of this analysis is to address the subsequent research questions:

- Among water-based nanofluids comprising of Cu, Al_2O_3 and TiO_2, which exhibits more pronounced velocity and temperature distributions due to inherent factors?
- Among water-based nanofluids comprising of Cu, Al_2O_3 and TiO_2, which demonstrates higher surface drags and heat transfer rates due to inherent factors?
- Between curved and flat surfaces, which surface type experiences predominant effects in terms of velocity and temperature distributions, surface drags, and heat transfer rates?

Problem statement

Assume the flow of nanofluids containing copper (Cu), alumina (Al_2O_3) and titanium dioxide (TiO_2) nanoparticles over a curved surface which is heated up with convective heating. The curved sheet stretches along primary direction, denoted by S, with velocity $u_w = aS$ such that $a > 0$. A magnetic field of strength B_0 along $R-$ direction is also taken into consideration. Furthermore, a hot working base fluid (water) having heat transfer coefficient h_f is taken into consideration. The reference temperature is denoted by T_f which is greater than the surface temperature T_w (i.e., $T_f > T_w$). Also, the volumetric fraction distribution of the surface is denoted by C_w and free stream is denoted by C_∞ as portrayed in Fig. 1. The subsequent conventions have been made to investigate the nanofluids flows:

- The nanofluids flows are affected by the chemical reactivity, Joule heating, and magnetic field.
- The curved surface is taken to be impermeable.
- The curved surface is kept hot with a hot working fluid.

Using above stated assumptions we have[51–53]:
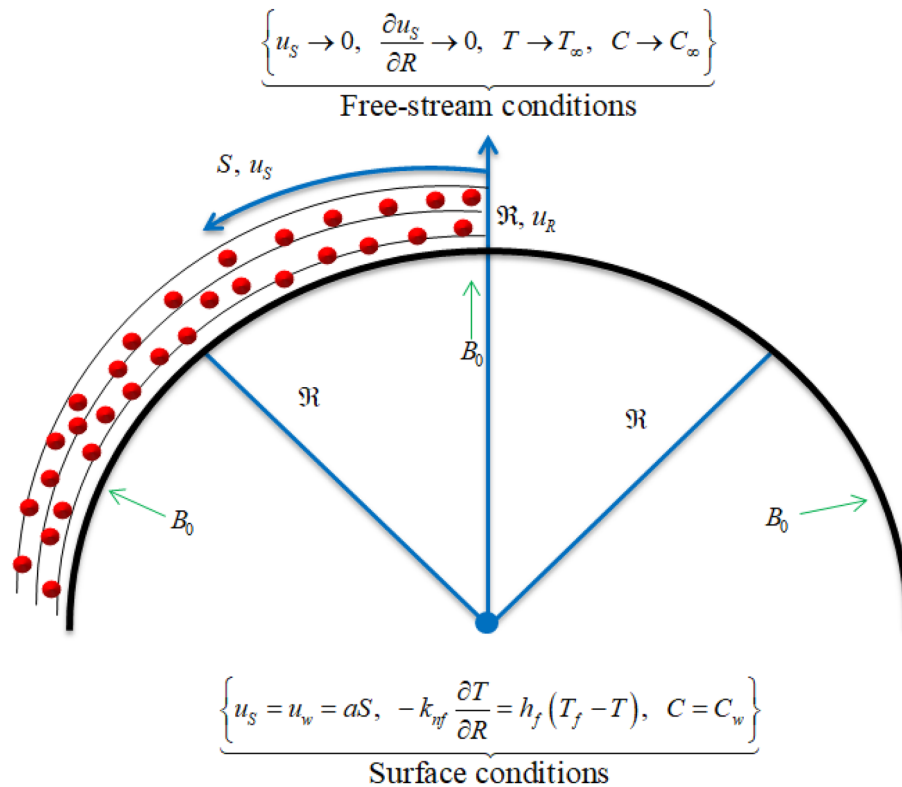
Figure 1. Graphical display of flow problem.

$$\frac{\partial((R + \Re)u_R)}{\partial R} + \Re \frac{\partial u_S}{\partial S} = 0, \tag{1}$$

$$\frac{u_S^2}{R + \Re} = \frac{1}{\rho_{nf}} \frac{\partial p}{\partial R}, \tag{2}$$

$$u_R \frac{\partial u_S}{\partial R} + \frac{\Re}{R + \Re} u_S \frac{\partial u_S}{\partial S} + \frac{u_S u_R}{R + \Re} = -\frac{1}{\rho_{nf}} \frac{\Re}{R + \Re} \frac{\partial p}{\partial S} + \frac{\mu_{nf}}{\rho_{nf}} \left(\frac{\partial^2 u_S}{\partial R^2} + \frac{1}{R + \Re} \frac{\partial u_S}{\partial R} - \frac{u_S}{(R + \Re)^2} \right) - \frac{\sigma_{nf} B_0^2}{\rho_{nf}} u_S, \tag{3}$$

$$u_R \frac{\partial T}{\partial R} + \frac{\Re}{R + \Re} u_S \frac{\partial T}{\partial S} = \frac{k_{nf}}{(\rho C_p)_{nf}} \left(\frac{\partial^2 T}{\partial R^2} + \frac{1}{R + \Re} \frac{\partial T}{\partial R} \right) + \frac{\sigma_{nf}}{(\rho C_p)_{nf}} B_0^2 u_S^2 + \frac{(\rho C_p)_p}{(\rho C_p)_{nf}} \left[D_B \frac{\partial C}{\partial R} \frac{\partial T}{\partial R} + \frac{D_T}{T_\infty} \left(\frac{\partial T}{\partial R} \right)^2 \right], \tag{4}$$

$$u_R \frac{\partial C}{\partial R} + \frac{\Re}{R + \Re} u_S \frac{\partial C}{\partial S} = D_B \left(\frac{\partial^2 C}{\partial R^2} + \frac{1}{R + \Re} \frac{\partial C}{\partial R} \right) + \frac{D_T}{T_\infty} \left(\frac{\partial^2 T}{\partial R^2} + \frac{1}{R + \Re} \frac{\partial T}{\partial R} \right) - K_r(C - C_\infty), \tag{5}$$

The constraints at boundaries are[53]:

$$\left\{ \begin{array}{l} u_S = aS = u_w, \quad u_R = 0, \quad C = C_w, \quad -k_{nf} \dfrac{\partial T}{\partial R} = h_f (T_f - T), \quad \text{at } R = 0, \\[2mm] u_S \to 0, \quad \dfrac{\partial u_S}{\partial R} \to 0, \quad C \to C_\infty, \quad T \to T_\infty, \quad \text{as } R \to \infty. \end{array} \right\} \tag{6}$$

The thermophysical features of the nanofluid are:

$$\left\{ \begin{array}{l} \dfrac{\mu_{nf}}{\mu_f} = \dfrac{1}{(1 - \Pi)^{2.5}}, \quad \dfrac{\rho_{nf}}{\rho_f} = (1 - \Pi) + \Pi \dfrac{\rho_s}{\rho_f}, \quad \dfrac{(\rho C_p)_{nf}}{(\rho C_p)_f} = (1 - \Pi) + \Pi \dfrac{(\rho C_p)_s}{(\rho C_p)_f}, \\[3mm] \dfrac{k_{nf}}{k_f} = \dfrac{k_s - 2\Pi (k_f - k_s) + 2k_f}{k_s + \Pi (k_f - k_s) + 2k_f}, \quad \dfrac{\sigma_{nf}}{\sigma_f} = \dfrac{\sigma_s + 2\sigma_f - 2\Pi (\sigma_f - \sigma_s)}{\sigma_s + 2\sigma_f + \Pi (\sigma_f - \sigma_s)}. \end{array} \right\} \tag{7}$$

Table 1 depicts the measured values of pure fluid and nanoparticles.

To convert the equations mentioned earlier, the similarity variables are established as follows:

4

Properties	ρ[J/kg K]	C_p[kg/m³]	k[W/m K]	σ [S/m]
H_2O	997.1	4179	0.613	5.5×10^{-6}
TiO_2	4250	686.2	8.9538	2.38×10^6
Cu	8933	385	400	1163.10×10^7
Al_2O_3	3970	765	46	131.70×10^7

Table 1. Measured values of the base fluid and nanoparticles in the experiment[54–56].

$$\begin{cases} \Gamma = R\sqrt{\dfrac{a}{\nu_f}}, \quad u_S = aSf'(\Gamma), \quad u_R = -\dfrac{\Re}{R+\Re}\sqrt{a\nu_f}f(\Gamma), \\ p = \rho_f(aS)^2 P(\Gamma), \quad \varphi(\Gamma) = \dfrac{C-C_\infty}{C_w-C_\infty}, \ \theta(\Gamma) = \dfrac{T-T_\infty}{T_f-T_\infty} \end{cases}, \tag{8}$$

By utilizing the similarity variables mentioned above, Eq. (1) is obvious, and Eq. (2) converted to:

$$\frac{\rho_f}{\rho_{nf}}P'(\Gamma) = \frac{1}{\alpha}f'^2(\Gamma), \tag{9}$$

where $\alpha = \Gamma + \delta$. Equation (3) can be reduced as:

$$\frac{\rho_f}{\rho_{nf}}\left(\frac{2\delta}{\alpha}\right)P(\Gamma) = \begin{cases} \left(\dfrac{\mu_{nf}/\mu_f}{\rho_{nf}/\rho_f}\right)\left(f'''(\Gamma)+f''(\Gamma)\left(\dfrac{1}{\alpha}\right)-f'(\Gamma)\left(\dfrac{1}{\alpha^2}\right)\right)-f'^2(\Gamma)\left(\dfrac{\delta}{\alpha}\right) \\ -\left(\dfrac{\sigma_{nf}/\sigma_f}{\rho_{nf}/\rho_f}\right)f'(\Gamma)M + f''(\Gamma)f(\Gamma)\left(\dfrac{\delta}{\alpha}\right)+f'(\Gamma)\left(\dfrac{\delta}{\alpha^2}\right)f(\Gamma) \end{cases}. \tag{10}$$

By taking the derivative of Eq. (10) with respect to Γ and is incorporating it into Eq. (9), we derive:

$$\left(\frac{\mu_{nf}/\mu_f}{\rho_f/\rho_f}\right)\left[f^{iv}(\Gamma)+f'''(\Gamma)\left(\frac{2}{\alpha}\right)-f''(\Gamma)\left(\frac{1}{\alpha^2}\right)+\left(\frac{1}{\alpha^3}\right)f'(\Gamma)\right]-\frac{\sigma_{nf}/\sigma_f}{\rho_{nf}/\rho_f}M\left[f'(\Gamma)\left(\frac{1}{\alpha}\right)+f''(\Gamma)\right]$$
$$+\left(\frac{\delta}{\alpha}\right)\left[f'''(\Gamma)f(\Gamma)-f''(\Gamma)f'(\Gamma)\right]+\left(\frac{\delta}{\alpha^2}\right)\left[f''(\Gamma)f(\Gamma)-f'^2(\Gamma)\right]-\left(\frac{\delta}{\alpha^3}\right)f'(\Gamma)f(\Gamma)=0, \tag{11}$$

While rest of the main equations are converted as

$$\frac{1}{\Pr}\frac{k_{nf}/k_f}{(\rho C_p)_{nf}/(\rho C_p)_f}\left[\theta''(\Gamma)+\left(\frac{1}{\alpha}\right)\theta'(\Gamma)\right]+\left(\frac{\delta}{\alpha}\right)\theta'(\Gamma)f(\Gamma)+$$
$$Nt\theta'^2(\Gamma)+Nb\varphi'(\Gamma)\theta'(\Gamma)+\frac{\sigma_{nf}/\sigma_f}{(\rho C_p)_{nf}/(\rho C_p)_f}MEcf'^2(\Gamma)=0. \tag{12}$$

$$\phi''(\Gamma)+\left(\frac{1}{\alpha}\right)\phi'(\Gamma)+\left(\frac{Nt}{Nb\alpha}\right)\theta'(\Gamma)+\left(\frac{\Gamma Sc}{\alpha}\right)\phi'(\Gamma)f(\Gamma)+\frac{Nt}{Nb}\theta''(\Gamma)-Sc\gamma\phi(\Gamma)=0. \tag{13}$$

$$\begin{cases} f'(0)=1, \ f(0)=0, \ \theta'(0)=\dfrac{Bi}{k_{nf}/k_f}(\theta(0)-1), \ \phi(0)=1, \\ f'(\infty)\to 0, \ f''(\infty)\to 0, \ \theta(\infty)\to 0, \ \phi(\infty)\to 0. \end{cases} \tag{14}$$

Pressure can be reduced as:

$$P(\Gamma) = \left(\frac{\alpha}{2\delta}\right)\begin{bmatrix} \dfrac{\mu_{nf}}{\mu_f}\left(f'''(\Gamma)+\left(\dfrac{1}{\alpha}\right)f''(\Gamma)-\left(\dfrac{1}{\alpha^2}\right)f'(\Gamma)\right)-\left(\dfrac{\sigma_{TH}}{\sigma_f}\right)f'(\Gamma)M+ \\ \dfrac{\rho_{nf}}{\rho_f}\left(\dfrac{\delta}{\alpha}\right)f''(\Gamma)f(\Gamma)+\dfrac{\rho_{nf}}{\rho_f}\left(\dfrac{\delta}{\alpha^2}\right)f'(\Gamma)f(\Gamma)-\left(\dfrac{\delta}{\alpha}\right)\left(\dfrac{\rho_{nf}}{\rho_f}\right)f'^2(\Gamma). \end{bmatrix} \tag{15}$$

$$\left\{\begin{array}{l} \delta = \sqrt{\dfrac{a}{\nu_f}}\Re, \quad M = \dfrac{\sigma_f B_0^2}{\rho_f a}, \quad Ec = \dfrac{u_S^2}{(C_p)_f(T_f - T_\infty)}, \quad \gamma = \dfrac{K_r}{a}, \quad \Pr = \dfrac{(\rho C_p)_f \nu_f}{k_f}, \\[3mm] Bi = \dfrac{h_f}{k_f}\sqrt{\dfrac{\nu_f}{a}}, \quad Nb = \dfrac{(C_w - C_\infty)D_B(\rho C_p)_p}{\nu_f(\rho C_p)_f}, \quad Nt = \dfrac{D_T(T_f - T_\infty)(\rho C_p)_p}{\nu_f T_\infty(\rho C_p)_f}, \quad Sc = \dfrac{\nu_f}{D_B}. \end{array}\right\} \tag{16}$$

In Eq. (16), δ shows the curvature factor, M shows magnetic factor, Bi is thermal Biot number, Ec is Eckert number, γ signifies chemically reactive factor, Nb is Brownian motion parameter, Nt presents the thermophoresis factor, Sc designates Schmidt number and $\Pr$ shows Prandtl number.

Main quantities are depicted as:

$$C_f = \frac{\tau_{RS}}{\rho_f S^2 a^2}, \quad Nu_S = \frac{Sq_w}{k_f(T_f - T_\infty)}, \quad Sh_S = -\frac{Sq_m}{D_B(C_w - C_\infty)}, \tag{17}$$

where

$$\tau_{RS} = \mu_{nf}\left(\frac{\partial u}{\partial R} - \frac{u}{R + \Re}\right)\bigg|_{R=0}, \quad q_w = -k_{nf}\frac{\partial T}{\partial R}\bigg|_{R=0}, \quad q_m = -D_B\frac{\partial C}{\partial R}\bigg|_{R=0}. \tag{18}$$

Using Eq. (8) in Eq. (17) we have

$$\left\{\begin{array}{l} \sqrt{\mathrm{Re}_S}\,C_{Ss} = \dfrac{\mu_{nf}}{\mu_f}\left(f''(0) - \dfrac{1}{\delta}f'(0)\right), \\[3mm] \dfrac{Nu_S}{\sqrt{\mathrm{Re}_S}} = -\dfrac{k_{nf}}{k_f}\theta'(0), \\[3mm] Sh = \dfrac{Sh_S}{\sqrt{\mathrm{Re}_S}} = -\varphi'(0). \end{array}\right\} \tag{19}$$

where $\mathrm{Re}_S = \frac{aS^2}{\nu_f}$ is local Reynolds number.

Solution by HAM

For the application of HAM, we introduced the initial guesses and linear operators as follows:

$$f_0(\Gamma) = 1 - e^{-\Gamma}, \quad \theta_0(\Gamma) = \frac{Bi}{\frac{k_{nf}}{k_f} + Bi}e^{-\Gamma}, \quad \phi_0(\Gamma) = e^{-\Gamma}, \tag{20}$$

$$L_f(\Gamma) = f^{iv} - f'', \quad L_\theta(\Gamma) = \theta'' - \theta, \quad L_\phi(\Gamma) = \phi'' - \phi, \tag{21}$$

with properties:

$$L_f\left(\sigma_1 + \sigma_2\Gamma + \sigma_3 e^{-\Gamma} + \sigma_4 e^{\Gamma}\right) = 0, \quad L_\theta\left(\sigma_5 e^{-\Gamma} + \sigma_6 e^{\Gamma}\right) = 0, \quad L_\phi\left(\sigma_7 e^{-\Gamma} + \sigma_8 e^{\Gamma}\right) = 0, \tag{22}$$

Above $\sigma_1 - \sigma_8$ are fixed values. For further applications of HAM, please see[57–59].

Convergence analysis

This section presents the convergence analysis of the applied method called HAM. This method has a convergence control parameter $\hbar$ which regulates the convergence of HAM. Figure 2 is exhibited to see the convergence area of velocity, temperature and volume fraction distributions. From Fig. 2, we confirm that the convergence of velocity takes place on interval $-1.0 \leq \hbar_f \leq 0.0$, convergence of thermal panels occur in $-2.3 \leq \hbar_\theta \leq 0.25$, and volume fraction distribution converges in $-2.7 \leq \hbar_\phi \leq 0.5$.

Code confirmation

This section is presented to validate our outcomes with earlier available results. The obtained results are determined for $-\sqrt{\mathrm{Re}_S}\,C_{fS}$ while varying δ and $M = \Pi = 0$. The results are presented in Table 2. From this Table, we have confirmed that the results obtained for a special case are in good relation with those published results.

Results and discussion

This section offers the physical debate of the consequences attained during this analysis. In this study hybrid nanofluid consisting of copper, alumina and titanium nanoparticles on a curved surface has investigated with impact of chemical reactivity, magnetic field and Joule heating. The curved surface is kept hot with a hot working fluid. The curved surface is taken to be impermeable. The HAM method is used to calculate the results for different flow profiles via different embedded factors. The obtained results are exhibited in Figs. 3, 4, 5, 6, 7, 8, 9, 10, 11, 12, 13, and 14, and Tables 3 and 4. The impression of curvature factor (δ) on velocity profiles ($f'(\Gamma)$) of Al_2O_3-nanofluid, Cu-nanofluid, and TiO_2-nanofluid is shown in Fig. 3. Higher δ increases the velocity profiles of all three types of fluids. The reason is that the increasing δ means that the curvature of the surface readuces or increases the radius of curvature which makes the surafce flatten. As the surface become flatten then the
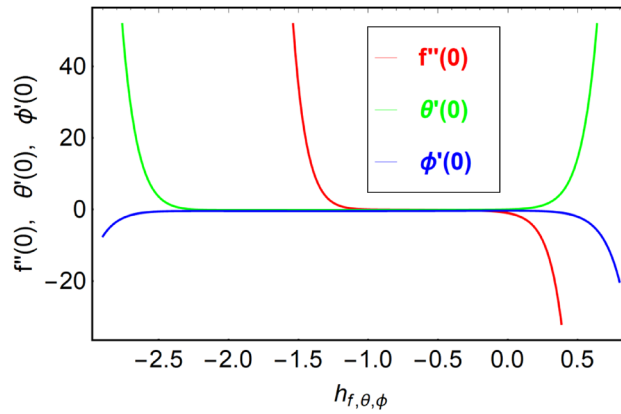
Figure 2. $\hbar-$ curves for $f''(0), \theta'(0)$ and $\phi'(0)$.

| δ	Rosca and Pop[60]	Current outcomes
5	1.15076	1.157565
10	1.07172	1.072534
20	1.03501	1.035464
30	1.02315	1.023463
40	1.01729	1.017346
50	1.01380	1.013995
100	1.00687	1.006963

Table 2. Comparison of $-\sqrt{\text{Re}_S}C_{fS}$ for different values of δ with $M = \Pi = 0$.
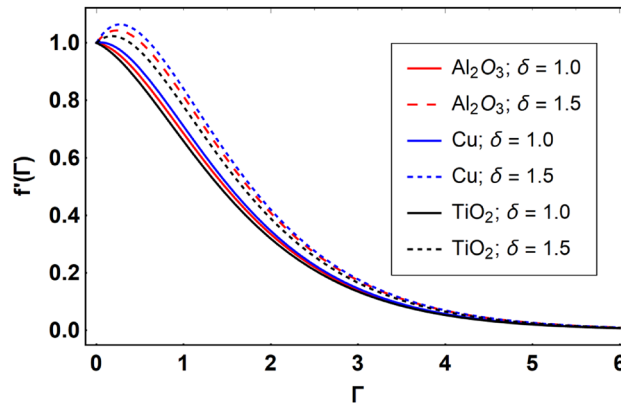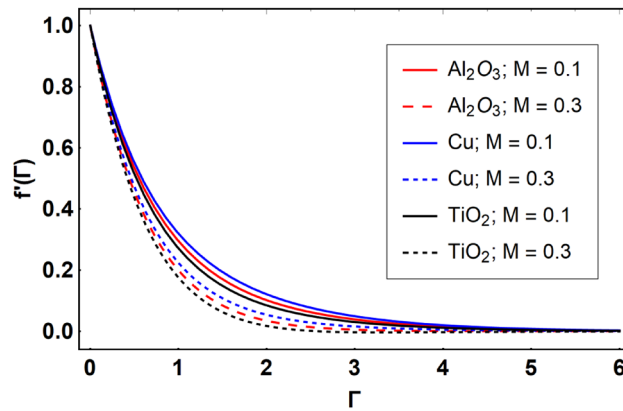

Figure 3. Effect of δ on $f'(\Gamma)$, when $\Pi = 0.04$, $M = 0.5$, $Ec = 0.1$, $\gamma = 0.5$, $Nb = 0.1$, $Nt = 0.1$, $Sc = 1.0$, $Bi = 0.5$ and $\text{Pr} = 6.2$.

opposing force at the flatten surface lowers which results higher velocity. The obtained results are investigated in the existence of magnetic field which means that the electrical conductivities of the different nanomaterials (i.e., Al_2O_3, Cu, and TiO_2) has significant role here. From the obtained results, we can see that the Cu-nanofluid has greater velocity than those of Al_2O_3 and TiO_2-nanofluids. The impact δ on temperature profiles ($\theta(\Gamma)$) of Al_2O_3-nanofluid, Cu-nanofluid, and TiO_2-nanofluid is portrayed in Fig. 4. An expansion in values of δ increases the temperature profiles of Al_2O_3-nanofluid, Cu-nanofluid, and TiO_2-nanofluid. Physically, the curvature factor and kinematic viscosity are inversually proportional to each other which means that the higher curvature factor reduces the kinematic viscosity which results enhancement in $\theta(\Gamma)$. Hence, the higher δ increases $\theta(\Gamma)$. Since from Table 1, we know that the thermal conductivities of the different nanomaterials (i.e., Al_2O_3, Cu, and TiO_2) has significant role here. From the obtained results, we can see that the Cu-nanofluid has greater thermal conductivity than those of Al_2O_3 and TiO_2-nanofluids. Therefore, Cu-nanofluid has greater thermal distribution than those of Al_2O_3 and TiO_2-nanofluids. The impact of M on $f'(\Gamma)$ for Al_2O_3-nanofluid, Cu-nanofluid, and
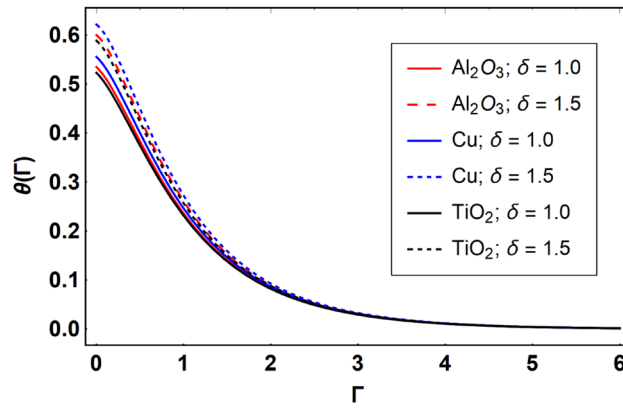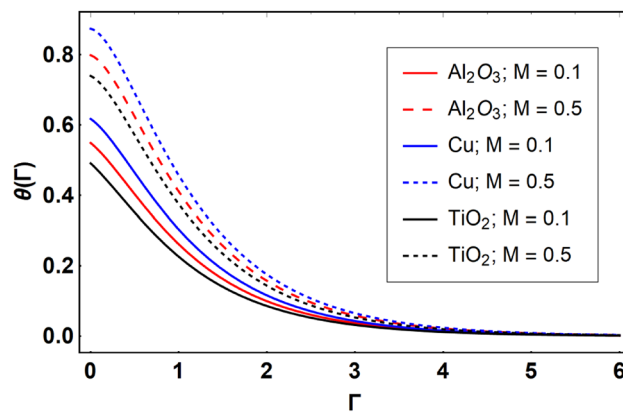
Figure 4. Effect of δ on $\theta(\Gamma)$, when $\Pi = 0.04, M = 0.5, Ec = 0.1, \gamma = 0.5, Nb = 0.1, Nt = 0.1, Sc = 1.0, Bi = 0.5$ and $\Pr = 6.2$.
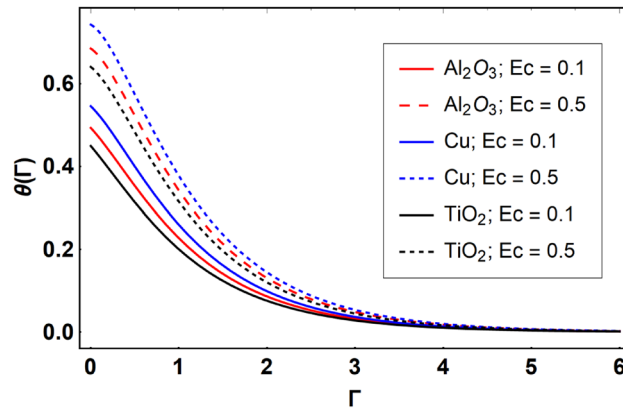

Figure 5. Effect of M on $f'(\Gamma)$, when $\Pi = 0.04 \, \delta = 5.0, Ec = 0.1, \gamma = 0.5, Nb = 0.1, Nt = 0.1, Sc = 1.0, Bi = 0.5$ and $\Pr = 6.2$.
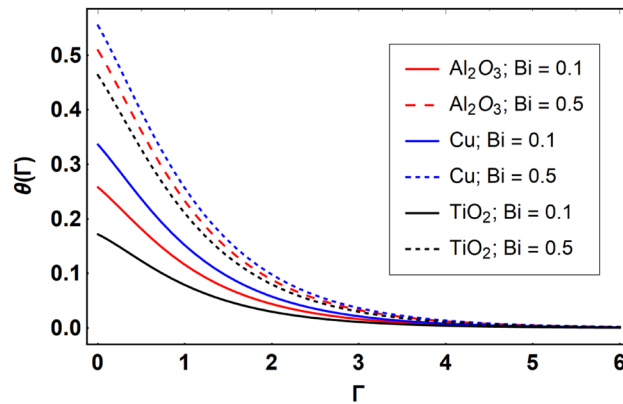

Figure 6. Effect of M on $\theta(\Gamma)$, when $\Pi = 0.04 \, \delta = 5.0, Ec = 0.1, \gamma = 0.5, Nb = 0.1, Nt = 0.1, Sc = 1.0, Bi = 0.5$ and $\Pr = 6.2$.

TiO$_2$-nanofluid is depicted in Fig. 5. The greater values of M reduces the velocity profiles of Al$_2$O$_3$-nanofluid, Cu-nanofluid, and TiO$_2$-nanofluid. Physically, when we increase the magnetic factor, a Lorentz force is created which opposes the motion of fluid particles. This opposing force increases for growth in skin friction at the sheet surface and reduced velocity distribution. The electrical conductivities of the different nanomaterials (i.e., Al$_2$O$_3$, Cu, and TiO$_2$) has significant role here. From the obtained results, we can see that the Cu-nanofluid has greater
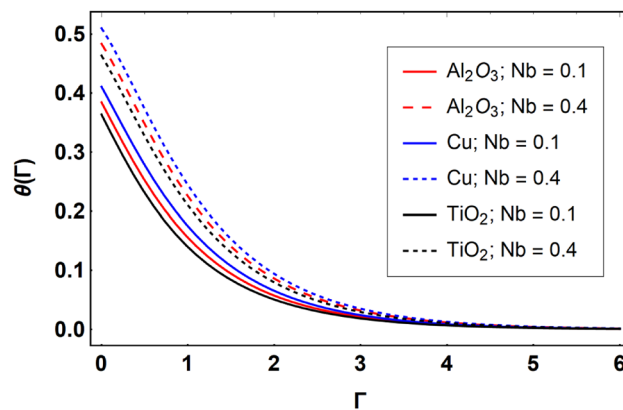
Figure 7. Effect of Ec on $\theta(\Gamma)$, when $\Pi = 0.04\, \delta = 5.0, M = 0.5, \gamma = 0.5, Nb = 0.1, Nt = 0.1, Sc = 1.0,$ $Bi = 0.5$ and $\mathrm{Pr} = 6.2$.
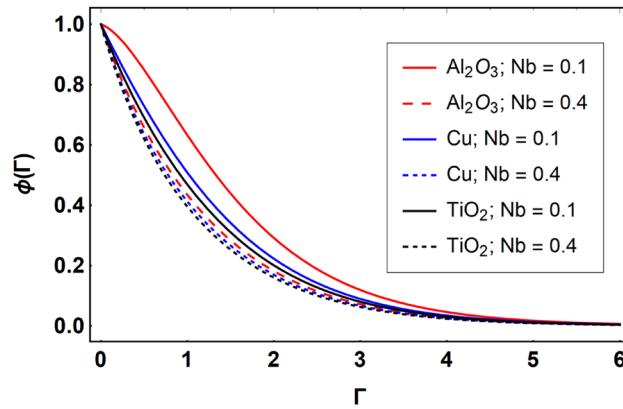

Figure 8. Effect of Bi on $\theta(\Gamma)$, when $\Pi = 0.04\, \delta = 5.0, M = 0.5, Ec = 0.1, \gamma = 0.5, Nb = 0.1, Nt = 0.1,$ $Sc = 1.0$ and $\mathrm{Pr} = 6.2$.
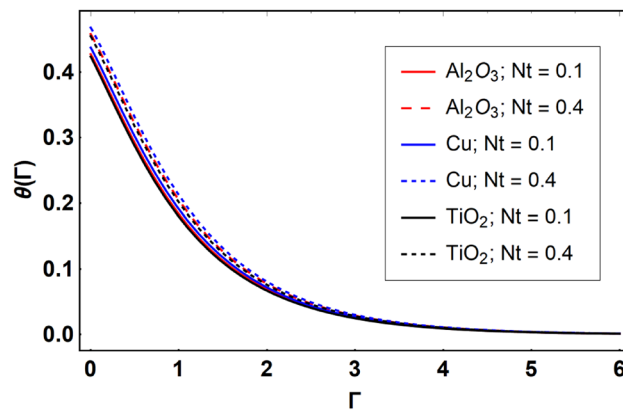

Figure 9. Effect of Nb on $\theta(\Gamma)$, when $\Pi = 0.04\, \delta = 5.0, M = 0.5, Ec = 0.1, \gamma = 0.5, Nt = 0.1, Sc = 1.0,$ $Bi = 0.5$ and $\mathrm{Pr} = 6.2$.
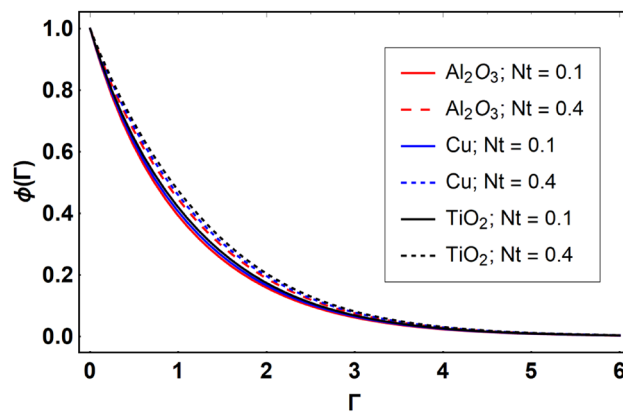
electrical conductivity than those of Al_2O_3 and TiO_2-nanofluids. Therefore, the Cu-nanofluid has greater velocity than those of Al_2O_3 and TiO_2-nanofluids. The impact of M on $\theta(\Gamma)$ of the Al_2O_3-nanofluid, Cu-nanofluid, and TiO_2-nanofluid is exposed in Fig. 6. The greater values of M increases the temperature profiles of Al_2O_3-nanofluid, Cu-nanofluid, and TiO_2-nanofluid. As the magnetic strength intensifies, the friction force on the sheet surface rises, leading to a higher rate of thermal transference attributed to increased friction. The higher rate of heat

Figure 10. Effect of Nb on $\phi(\Gamma)$, when $\Pi = 0.04\,\delta = 5.0$, $M = 0.5$, $Ec = 0.1$, $\gamma = 0.5$, $Nt = 0.1$, $Sc = 1.0$, $Bi = 0.5$ and $\Pr = 6.2$.

Figure 11. Effect of Nt on $\theta(\Gamma)$, when $\Pi = 0.04\,\delta = 5.0$, $M = 0.5$, $Ec = 0.1$, $\gamma = 0.5$, $Nb = 0.1$, $Sc = 1.0$, $Bi = 0.5$ and $\Pr = 6.2$.
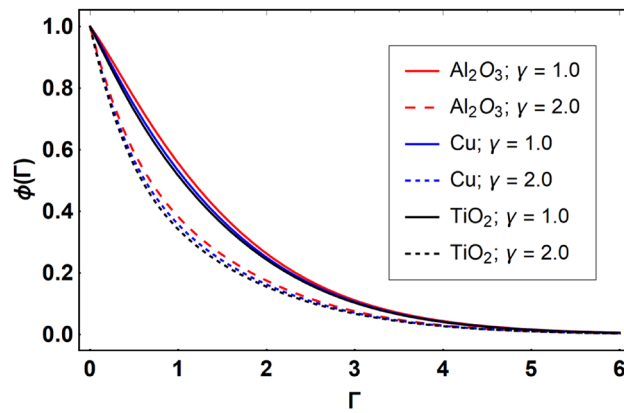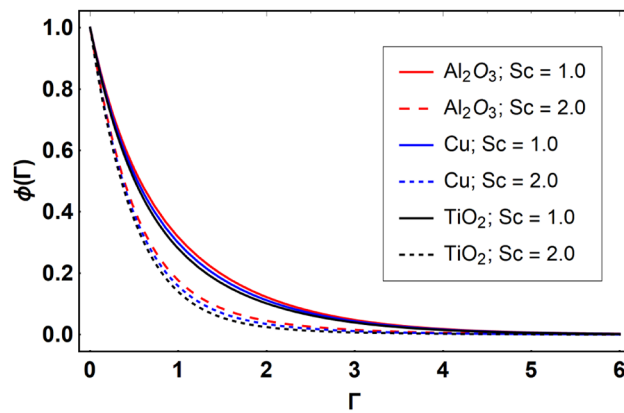

Figure 12. Effect of Nt on $\phi(\Gamma)$, when $\Pi = 0.04\,\delta = 5.0$, $M = 0.5$, $Ec = 0.1$, $\gamma = 0.5$, $Nb = 0.1$, $Sc = 1.0$, $Bi = 0.5$ and $\Pr = 6.2$.

transfer increases the temperature profiles of the nanofluids. Since, Cu-nanofluid has greater electrical conductivity so it will have greater resistive force and rate of heat transfer as well. Therefore, Cu-nanofluid has greater thermal distribution than those of Al_2O_3 and TiO_2-nanofluids. The impression Ec on thermal profiles for Al_2O_3-nanofluid, Cu-nanofluid, and TiO_2-nanofluid is shown in Fig. 7. Greater Ec is responsible for upsurge in $\theta(\Gamma)$ for Al_2O_3-nanofluid, Cu-nanofluid and TiO_2-nanofluid. The higher Ec transmits the kinetic energy into

10

Figure 13. Effect of γ on $\phi(\Gamma)$, when $\Pi = 0.04\,\delta = 5.0$, $M = 0.5$, $Ec = 0.1$, $Nb = 0.1$, $Nt = 0.1$, $Sc = 1.0$, $Bi = 0.5$ and $Pr = 6.2$.

Figure 14. Effect of Sc on $\phi(\Gamma)$, when $\Pi = 0.04\,\delta = 5.0$, $M = 0.5$, $Ec = 0.1$, $\gamma = 0.5$, $Nb = 0.1$, $Nt = 0.1$, $Bi = 0.5$ and $Pr = 6.2$.

internal heat energy due to viscous forces which results higher trnasfer rate of heat. Therefore, the Ec upsurges the temperature profiles for all types of fluids. Comparing the three different nanofluids (i.e., Al_2O_3-nanofluid, Cu-nanofluid, and TiO_2-nanofluid), the Cu-nanofluid flow has higher temperature than those of Al_2O_3-nanofluid and TiO_2-nanofluid. Actually, Cu nanomaterial has greater thermal conductance than those of Al_2O_3 and TiO_2 nanomaterials. The impression of Bi (Thermal Biot number) on thermal profiles of the Al_2O_3-nanofluid, Cu-nanofluid, and TiO_2-nanofluid is shown in Fig. 8. Growth in Bi increase the thermal profiles of Al_2O_3-nanofluid, Cu-nanofluid and TiO_2-nanofluid. The higher Bi upsurges the coefficient of thermal tranefernce that supports thegrowth in width of thermal layer at boundary. Therefore, the higher Bi increases $\theta(\Gamma)$ for Al_2O_3-nanofluid, Cu-nanofluid and TiO_2-nanofluid. Comparing the three different nanofluids, we see that Cu-nanofluid flow has higher temperature than those of Al_2O_3-nanofluid and TiO_2-nanofluid. Actually, Cu nanomaterial has better conductance of heat than those of Al_2O_3 and TiO_2 nanomaterials. The impact of Nb (Brownian motion factor) on thermal and volume fraction distributions on all three types of nanofluid is shown in Figs. 9 and 10. Augmentation in Nb supports thermal distributions while reduce the volume fraction distributions of all three types of fluids. The higher Nb increases the width of thermal layer at boundary, which resutls higher temperature distribution. Since Cu nanomaterial has better conductance of heat than those of Al_2O_3 and TiO_2 nanomaterials, so Cu-nanofluid has a greater $\theta(\Gamma)$. Conversely, higher values of Nb reduce volume fraction distributions of the Al_2O_3-nanofluid, Cu-nanofluid, and TiO_2-nanofluid. Actually, greater Nb diminishes boundary layer thickness of the volume fraction distribution and causes a drop in the respective profiles of the the Al_2O_3-nanofluid, Cu-nanofluid, and TiO_2-nanofluid. Comparing the three different nanofluids we see that Cu-nanofluid flow has higher temperature than those of Al_2O_3-nanofluid and TiO_2-nanofluid. The impression of thermophoretic factor (Nt) on thermal and volume fraction panels for all three types of fluids is shown in Figs. 11 and 12. From the Figures, we see that the greater Nt increases the thermal and volume fraction distributions of the Al_2O_3-nanofluid, Cu-nanofluid and TiO_2-nanofluid. Actually, the greater Nt shows that the thermophoretic forces moves the fluid particles from hotter to colder regions which results higher thermal distribution of the nanofluids flows. Also, the greater Nt increases the volume fraction distribution of the nanofluids flows. Comparing the three different nanofluids (i.e., Al_2O_3-nanofluid, Cu-nanofluid, and TiO_2-nanofluid), the Cu-nanofluid flow has higher

Π	M	Ec	Nb	Nt	Bi	$\frac{Nu_s}{\sqrt{Re_s}}$		
						Cu nanofluid	*Al₂O₃* nanofliud	*TiO₂* nanofluid
0.01						1.224355	1.186543	1.153257
0.02						1.234567	1.196756	1.160753
0.03						1.247648	1.205323	1.170853
0.04						1.253268	1.219638	1.189518
	0.1					0.286474	0.254363	0.225432
	0.2					0.297453	0.269538	0.236851
	0.3					0.306426	0.275373	0.240763
		0.3				0.257563	0.244752	0.228653
		0.6				0.264538	0.259642	0.238532
		0.9				0.274326	0.260864	0.249769
			0.1			0.453353	0.425326	0.387537
			0.2			0.432156	0.406537	0.369633
			0.3			0.415653	0.386273	0.346854
				0.1		0.286463	0.257533	0.236747
				0.2		0.297537	0.268942	0.240863
				0.3		0.305356	0.278095	0.258525
					0.1	0.554535	0.458958	0.415784
					0.2	0.594371	0.497446	0.459048
					0.3	0.647964	0.543589	0.490637

Table 3. Impacts of *M*, *Ec*, *Nb*, *Nt*, *Bi* and Π on $\frac{Nu_S}{\sqrt{Re_S}}$.

Nb	Nt	Sc	$\frac{Sh_s}{\sqrt{Re_s}}$
0.1			1.685457
0.2			1.697428
0.3			1.708637
	0.1		1.635685
	0.2		1.654374
	0.3		1.679075
		0.1	1.457643
		0.2	1.445784
		0.3	1.435895

Table 4. Sherwood number for variations in *Nb* and *Nt*.

temperature and volume fraction distributions than those of Al_2O_3-nanofluid and TiO_2-nanofluid. The impression of chemical reactivity factor (γ) on volume fraction distributions of the Al_2O_3-nanofluid, Cu-nanofluid, and TiO_2-nanofluid is shown in Fig. 13. From this Figure, we see that the greater γ reduces the volume fraction distributions for all three kinds of fluids. The greater γ reduces the volumetric boundary layer thickness which results a reduced volume fraction distributions of the Al_2O_3-nanofluid, Cu-nanofluid and TiO_2-nanofluid. Comparing the three different nanofluids (i.e., Al_2O_3-nanofluid, Cu-nanofluid, and TiO_2-nanofluid), the Cu-nanofluid flow has volume fraction distributions than those of Al_2O_3-nanofluid and TiO_2-nanofluid. The impact of Schmidt number (Sc) on volume fraction distributions of the Al_2O_3-nanofluid, Cu-nanofluid, and TiO_2-nanofluid is shown in Fig. 14. From this Figure, we see that the greater Sc reduces the volume fraction distributions of the Al_2O_3-nanofluid, Cu-nanofluid and TiO_2-nanofluid. The greater Sc reduces the Brownian diffusivity of the nanofluids flows which result the decreasing volumetric boundary layer thickness. Therefore, the reduced volume fraction distributions of the Al_2O_3-nanofluid, Cu-nanofluid and TiO_2-nanofluid are found here. Comparing the three different nanofluids (i.e., Al_2O_3-nanofluid, Cu-nanofluid, and TiO_2-nanofluid), the Cu-nanofluid flow has higher volume fraction distributions than those of Al_2O_3-nanofluid and TiO_2-nanofluid. Table 3 shows the variation in heat transfer rate $\frac{Nu_s}{\sqrt{Re_s}}$ of the three different nanofluids (i.e., Al_2O_3-nanofluid, Cu-nanofluid, and TiO_2-nanofluid) via Π, *M*, *Ec*, *Nb*, *Nt* and *Bi*. From the obtained results, we have found that $\frac{Nu_s}{\sqrt{Re_s}}$ increases via Π, *M*, *Ec*, *Bi* and *Nt* while reduces via *Nb*. Physically, the higher values of Π increase the thermal conductivities of the nanofluids which results higher rate of heat transfers. Comparing the three different nanofluids (i.e., Al_2O_3-nanofluid, Cu-nanofluid, and TiO_2-nanofluid), the Cu-nanofluid flow has higher volume fraction distributions than those of Al_2O_3-nanofluid and TiO_2-nanofluid. Table 4 shows the variation in mass transfer rate $\frac{Nu_s}{\sqrt{Re_s}}$

of the three different nanofluids (i.e., Al$_2$O$_3$-nanofluid, Cu-nanofluid, and TiO$_2$-nanofluid) via Nb, Nt and Sc. From the obtained results, we havefound that $\frac{Nu_{\bar{s}}}{\sqrt{Re_s}}$ increases via Nb and Nt while reduces via Sc.

Conclusion

In this study hybrid nanofluid consisting of copper, alumina and titanium nanoparticles on a curved sheet has investigated with impact of chemical reactivity, magnetic field and Joule heating. The leading equations have converted to normal equations by using appropriate set of variables and has then evaluated by homotopy analysis method (HAM). The results are shown through Figures and Tables and are discussed physically.

The ultimate results of the current analysis are:

- The velocity and temperature panels augmenting functions of curvature factor.
- Growing values of magnetic factor reduce the velocity profiles while opposite impact is found for the temperature distribution.
- Brownian motion factor, thermophoresis factor and thermal Biot, Eckert numbers have direct relations with the thermal distribution.
- The Brownian motion, chemical reactivity factors, and Schmidt number has inverse relation with the volume fraction distribution.
- The Cu-nanofluid flow has higher velocity, temperature, and volume fraction distributions than those of Al$_2$O$_3$-nanofluid and TiO$_2$-nanofluid.
- The Cu-nanofluid flow has higher heat and mass transference rates than those of Al$_2$O$_3$-nanofluid and TiO$_2$-nanofluid.

Data availability

The data that support the findings of this study are available from the corresponding author upon reasonable request.

References

1. Choi, S. & Eastman, J. Enhancing thermal conductivity of fluids with nanoparticles, accessed 10 September 2021 (1995). https://www.osti.gov/biblio/196525 (1995).
2. Pathak, S. K., Kumar, R., Goel, V., Pandey, A. K. & Tyagi, V. V. Recent advancements in thermal performance of nano-fluids charged heat pipes used for thermal management applications: A comprehensive review. *Appl. Therm. Eng.* **216**, 119023 (2022).
3. Alzahrani, J. *et al.* Evaluation of bioconvection for sinusoidally moving Jeffrey nanoparticles in view of temperature dependent thermal conductivity and Cattaneo–Christov heat diffusion model. *Ain Shams Eng. J.* **14**, 102124 (2023).
4. Hussain, S. M., Jamshed, W., Pasha, A. A., Adil, M. & Akram, M. Galerkin finite element solution for electromagnetic radiative impact on viscid Williamson two-phase nanofluid flow via extendable surface. *Int. Commun. Heat Mass Transf.* **137**, 106243 (2022).
5. Arshad, M. *et al.* Rotating hybrid nanofluid flow with chemical reaction and thermal radiation between parallel plates. *Nanomaterials* **12**, 1–20. https://doi.org/10.3390/nano12234177 (2022).
6. Uddin, M. J., Al-Balushi, J., Mahatabuddin, S. & Rahman, M. M. Convective heat transport for copper oxide-water nanofluid in an isosceles triangular cavity with a rippled base wall in the presence of magnetic field. *Int. J. Thermofluids.* **16**, 100195 (2022).
7. Kumar, P., Poonia, H., Ali, L. & Areekara, S. The numerical simulation of nanoparticle size and thermal radiation with the magnetic field effect based on tangent hyperbolic nanofluid flow. *Case Stud. Therm. Eng.* **37**, 102247 (2022).
8. Arshad, M. *et al.* Exploration of heat and mass transfer subjected to first order chemical reaction and thermal radiation: Comparative dynamics of nano, hybrid and tri-hybrid particles over dual stretching surface. *Int. Commun. Heat Mass Transf.* **146**, 106916 (2023).
9. Khan, A., Shah, Z., Alzahrani, E. & Islam, S. Entropy generation and thermal analysis for rotary motion of hydromagnetic Casson nanofluid past a rotating cylinder with Joule heating effect. *Int. Commun. Heat Mass Transf.* **119**, 104979 (2020).
10. Acharya, N., Mabood, F., Shahzad, S. A. & Badruddin, I. A. Hydrothermal variations of radiative nanofluid flow by the influence of nanoparticles diameter and nanolayer. *Int. Commun. Heat Mass Transf.* **130**, 105781. https://doi.org/10.1016/J.ICHEATMASSTRANSFER.2021.105781 (2022).
11. Arshad, M. *et al.* Heat and mass transfer analysis above an unsteady infinite porous surface with chemical reaction. *Case Stud. Therm. Eng.* **36**, 102140 (2022).
12. Arshad, M. & Hassan, A. A numerical study on the hybrid nanofluid flow between a permeable rotating system. *Eur. Phys. J. Plus.* **137**, 1126 (2022).
13. Arshad, M. *et al.* Effect of inclined magnetic field on radiative heat and mass transfer in chemically reactive hybrid nanofluid flow due to dual stretching. *Sci. Rep.* **13**, 7828 (2023).
14. Hussain, S. M. *et al.* Artificial neural network modeling of mixed convection viscoelastic hybrid nanofluid across a circular cylinder with radiation effect: Case study. *Case Stud. Therm. Eng.* **50**, 103487 (2023).
15. Nimmy, P. *et al.* Implication of radiation on the thermal behavior of a partially wetted dovetail fin using an artificial neural network. *Case Stud. Therm. Eng.* **51**, 103552 (2023).
16. Khan, S. U. *et al.* Implication of Arrhenius activation energy and temperature-dependent viscosity on non-Newtonian nanomaterial bio-convective flow with partial slip. *Arab. J. Sci. Eng.* https://doi.org/10.1007/s13369-021-06274-3 (2022).
17. Goud Bejawada, S. *et al.* Radiation effect on MHD Casson fluid flow over an inclined non-linear surface with chemical reaction in a Forchheimer porous medium. *Alex. Eng. J.* **61**, 8207–8220. https://doi.org/10.1016/J.AEJ.2022.01.043 (2022).
18. Asjad, M. I., Zahid, M., Inc, M., Baleanu, D. & Almohsen, B. Impact of activation energy and MHD on Williamson fluid flow in the presence of bioconvection. *Alex. Eng. J.* **61**, 8715–8727 (2022).
19. Dey, D., Makinde, O. D. & Borah, R. Analysis of dual solutions in MHD fluid flow with heat and mass transfer past an exponentially shrinking/stretching surface in a porous medium. *Int. J. Appl. Comput. Math.* **8**, 66 (2022).
20. Singh, J. K., Seth, G. S. & Hussain, S. M. Thermal performance of hydromagnetic nanofluid flow within an asymmetric channel with arbitrarily conductive walls filled with Darcy–Brinkman porous medium. *J. Magn. Magn. Mater.* **582**, 171034 (2023).

21. Mahabaleshwar, U. S., Sneha, K. N., Chan, A. & Zeidan, D. An effect of MHD fluid flow heat transfer using CNTs with thermal radiation and heat source/sink across a stretching/shrinking sheet. *Int. Commun. Heat Mass Transf.* **135**, 106080 (2022).

22. Abbas, A., Jeelani, M. B. & Alharthi, N. H. Darcy–Forchheimer relation influence on MHD dissipative third-grade fluid flow and heat transfer in porous medium with Joule heating effects: A numerical approach. *Processes* **10**, 906 (2022).

23. Kodi, R. & Mopuri, O. Unsteady MHD oscillatory Casson fluid flow past an inclined vertical porous plate in the presence of chemical reaction with heat absorption and Soret effects. *Heat Transf.* **51**, 733–752 (2022).

24. Hussain, S. M., Khan, U., Zaib, A., Ishak, A. & Sarris, I. E. Numerical computation of mixed convective entropy optimized in Darcy–Forchheimer flow of cross nanofluids through a vertical flat plate with irregular heat source/sink. *Tribol. Int.* **187**, 108757 (2023).

25. Raghunath, K., Gulle, N., Vaddemani, R. R. & Mopuri, O. Unsteady MHD fluid flow past an inclined vertical porous plate in the presence of chemical reaction with aligned magnetic field, radiation, and Soret effects. *Heat Transf.* **51**, 2742–2760 (2022).

26. Dawar, A., Khan, H., Islam, S. & Khan, W. The improved residual power series method for a system of differential equations: a new semi-numerical method. *Int. J. Model. Simul.* https://doi.org/10.1080/02286203.2023.2270884 (2023).

27. Reza-E-Rabbi, S. *et al.* Characterization of fluid flow and heat transfer of a periodic magnetohydrodynamics nano non-Newtonian liquid with Arrhenius activation energy and nonlinear radiation. *Heat Transf.* **51**, 6578–6615. https://doi.org/10.1002/HTJ.22614 (2022).

28. Goud, B. S. *et al.* Numerical case study of chemical reaction impact on MHD micropolar fluid flow past over a vertical riga plate. *Materials (Basel)* **15**, 4060 (2022).

29. Dawar, A., Wakif, A., Thumma, T. & Shah, N. A. Towards a new MHD non-homogeneous convective nanofluid flow model for simulating a rotating inclined thin layer of sodium alginate-based Iron oxide exposed to incident solar energy. *Int. Commun. Heat Mass Transf.* **130**, 105800 (2022).

30. Kalpana, G., Madhura, K. R. & Kudenatti, R. B. Numerical study on the combined effects of Brownian motion and thermophoresis on an unsteady magnetohydrodynamics nanofluid boundary layer flow. *Math. Comput. Simul.* **200**, 78–96 (2022).

31. Shahzad, A. *et al.* Brownian motion and thermophoretic diffusion impact on Darcy–Forchheimer flow of bioconvective micropolar nanofluid between double disks with Cattaneo–Christov heat flux. *Alex. Eng. J.* **62**, 1–15 (2023).

32. Tawade, J. V. *et al.* Effects of thermophoresis and Brownian motion for thermal and chemically reacting Casson nanofluid flow over a linearly stretching sheet. *Results Eng.* **15**, 100448. https://doi.org/10.1016/J.RINENG.2022.100448 (2022).

33. Upreti, H., Pandey, A. K., Uddin, Z. & Kumar, M. Thermophoresis and Brownian motion effects on 3D flow of Casson nanofluid consisting microorganisms over a Riga plate using PSO: A numerical study, Chinese. *J. Phys.* **78**, 234–270 (2022).

34. Khan, R. A. *et al.* Heat transfer between two porous parallel plates of steady nano fludis with Brownian and Thermophoretic effects: A new stochastic numerical approach. *Int. Commun. Heat Mass Transf.* **126**, 105436 (2021).

35. Ahmed, S., Xu, H., Zhou, Y. & Yu, Q. Modelling convective transport of hybrid nanofluid in a lid driven square cavity with consideration of Brownian diffusion and thermophoresis. *Int. Commun. Heat Mass Transf.* **137**, 106226 (2022).

36. Puneeth, V. *et al.* Implementation of modified Buongiorno's model for the investigation of chemically reacting rGO-Fe_3O_4-TiO_2-H_2O ternary nanofluid jet flow in the presence of bio-active mixers. *Chem. Phys. Lett.* **786**, 139194 (2022).

37. Rana, A., Reza, M., Prasad, K. M. & Shit, G. C. Effects of different viscous dissipation and Joule heating on electromagnetohydrodynamic flow of power-law fluid in the porous microchannel. *Int. J. Ambient Energy.* **44**, 765–779 (2023).

38. Rasool, G., Wang, X., Yashkun, U., Lund, L. A. & Shahzad, H. Numerical treatment of hybrid water based nanofluid flow with effect of dissipation and Joule heating over a shrinking surface: Stability analysis. *J. Magn. Magn. Mater.* **571**, 170587 (2023).

39. Faruk, M. O. *et al.* Functional textiles and composite based wearable thermal devices for Joule heating: Progress and perspectives. *Appl. Mater. Today.* **23**, 101025 (2021).

40. Hwang, D. *et al.* Development of a high heat flux electric joule heating system for testing a one-side heated cooling channel. *Fusion Sci. Technol.* **78**, 220–242 (2022).

41. Otman, H. A. *et al.* Mathematical analysis of mixed convective stagnation point flow over extendable porous riga plate with aggregation and joule heating effects. *Heliyon* **9**, e17538 (2023).

42. Irfan, M., Anwar, M. S., Kebail, I. & Khan, W. A. Thermal study on the performance of Joule heating and Sour-Dufour influence on nonlinear mixed convection radiative flow of Carreau nanofluid. *Tribol. Int.* **188**, 108789 (2023).

43. Prakash, J., Tripathi, D., Akkurt, N. & Bég, O. A. Tangent hyperbolic non-Newtonian radiative bioconvection nanofluid flow from a bi-directional stretching surface with electro-magneto-hydrodynamic, Joule heating and modified diffusion effects. *Eur. Phys. J. Plus.* **137**, 472 (2022).

44. Ajithkumar, M., Lakshminarayana, P. & Vajravelu, K. Diffusion effects on mixed convective peristaltic flow of a bi-viscous Bingham nanofluid through a porous medium with convective boundary conditions. *Phys. Fluids* **35**, 032008 (2023).

45. Khan, M. N. *et al.* Analysis of fluctuating heat and current density of mixed convection flow with viscosity and thermal conductivity effects along horizontal nonconducting cylinder. *Case Stud. Therm. Eng.* **46**, 103023 (2023).

46. Hamza, M. M., Abdulsalam, S. & Ahmad, S. K. Time-dependent magnetohydrodynamic (MHD) flow of an exothermic arrhenius fluid in a vertical channel with convective boundary condition. *Adv. Math. Phys.* https://doi.org/10.1155/2023/7173925 (2023).

47. Rashad, A. M., Nafe, M. A. & Eisa, D. A. Heat variation on MHD Williamson hybrid nanofluid flow with convective boundary condition and Ohmic heating in a porous material. *Sci. Rep.* **13**, 6071 (2023).

48. Baag, S., Panda, S., Pattnaik, P. K. & Mishra, S. R. Free convection of conducting nanofluid past an expanding surface with heat source with convective heating boundary conditions. *Int. J. Ambient Energy.* **44**, 880–891 (2023).

49. Humane, P. P., Patil, V. S., Shamshuddin, M. D., Rajput, G. R. & Patil, A. B. Role of bioconvection on the dynamics of chemically active Casson nanofluid flowing via an inclined porous stretching sheet with convective conditions. *Int. J. Model. Simul.* https://doi.org/10.1080/02286203.2022.2164156 (2023).

50. Prasad, K. V., Choudhari, R., Vaidya, H., Bhat, A. & Animasaun, I. L. Analysis of couple stress nanofluid flow under convective condition in the temperature-dependent fluid properties and Lorentz forces. *Heat Transf.* **52**, 216–235 (2023).

51. Nadeem, S., Abbas, N. & Malik, M. Y. Inspection of hybrid based nanofluid flow over a curved surface. *Comput. Methods Progr. Biomed.* https://doi.org/10.1016/j.cmpb.2019.105193 (2020).

52. Sarada, K. *et al.* Impact of exponential form of internal heat generation on water-based ternary hybrid nanofluid flow by capitalizing non-Fourier heat flux model. *Case Stud. Therm. Eng.* **38**, 102332 (2022).

53. Dawar, A., Islam, S., Shah, Z. & Mahmuod, S. R. A passive control of Casson hybrid nanofluid flow over a curved surface with alumina and copper nanomaterials: A study on sodium alginate-based fluid. *J. Mol. Liq.* **382**, 122018 (2023).

54. Abbas, W. & Magdy, M. M. Heat and mass transfer analysis of nanofluid flow based on, and over a moving rotating plate and impact of various nanoparticle shapes. *Math. Probl. Eng.* **2020** (2020).

55. Dawar, A., Islam, S., Shah, Z., Mahmuod, S. R. & Lone, S. A. Dynamics of inter-particle spacing, nanoparticle radius, inclined magnetic field and nonlinear thermal radiation on the water-based copper nanofluid flow past a convectively heated stretching surface with mass flux condition: A strong suction case. *Int. Commun. Heat Mass Transf.* **137**, 106286 (2022).

56. Dawar, A., Islam, S., Shah, Z. & Lone, S. A. Significance of the third-order slip flow of graphene-(100% water, 70% water+ 30% ethylene glycol, and 50% water+ 50% ethylene glycol) nanofluids flow over a stretching surface with a Cattaneo–Christov heat and mass flux model. *ZAMM J. Appl. Math. Mech. für Angew. Math. und Mech.* **102.**, e202200133 (2022).

57. Liao, S. Introduction, Homotopy Anal. Method Nonlinear Differ. Equations, pp. 3–14. https://doi.org/10.1007/978-3-642-25132-0_1 (2012).

58. Liao, S. *Beyond Perturbation: Introduction to the Homotopy Analysis Method* (Chapman and Hall/CRC, 2003).
59. Liao, S. J. *On the Proposed Homotopy Analysis Technique for Nonlinear Problems and its Applications* (Shanghai Jiao Tong University, 1992).
60. Roşca, N. C. & Pop, I. Unsteady boundary layer flow over a permeable curved stretching/shrinking surface. *Eur. J. Mech.* **51**, 61–67 (2015).

Acknowledgements

Author contributions

All authors are equally contributed.

Funding

Competing interests

The authors declare no competing interests.

Additional information

Correspondence and requests for materials should be addressed to G.B.

Reprints and permissions information is available at www.nature.com/reprints.

Publisher's note Springer Nature remains neutral with regard to jurisdictional claims in published maps and institutional affiliations.